

BIROn - Birkbeck Institutional Research Online

Diring, J. and Moulleron, S. and McDonald, Neil Q. and Treisman, R. (2019) RPEL family rhoGAPs link Rac/Cdc42 GTP loading to G-actin availability. *Nature Cell Biology* 21 , pp. 845-855. ISSN 1465-7392.

Downloaded from: <http://eprints.bbk.ac.uk/26778/>

Usage Guidelines:

Please refer to usage guidelines at <http://eprints.bbk.ac.uk/policies.html> or alternatively contact lib-eprints@bbk.ac.uk.

1 **RPEL family rhoGAPs link Rac/Cdc42 GTP loading to G-actin availability**

2

3

4

5 Jessica Diring¹, Stephane Mouilleron², Neil Q. McDonald^{3,4} and Richard Treisman^{*1,5}

6

7 ¹Signalling and Transcription Group

8 ²Structural Biology Science Technology Platform

9 ³Signalling and Structural Biology Group

10 The Francis Crick Institute, 1 Midland Road, London NW1 1AT, UK□

11

12 ⁴Institute of Structural and Molecular Biology, Department of Biological Sciences, Birkbeck

13 College, Malet Street, London, WC1E 7HX UK

14

15 ⁵Correspondence should be addressed to R.T. (email: richard.treisman@crick.ac.uk)

16

17 **SHORT TITLE:** Regulation of a rhoGAP by G-actin

18 **KEYWORDS:** RhoGAP, ArhGAP12, RPEL, MRTF, actin, GAP, melanoma, Rac, Cdc42

19

20 **ABSTRACT**

21 RPEL proteins, which contain the G-actin binding RPEL motif, coordinate cytoskeletal
22 processes with actin dynamics. We show that the ArhGAP12- and ArhGAP32-family
23 GTPase activating proteins are RPEL proteins. We determine the structure of the
24 ArhGAP12/G-actin complex, and show that G-actin contacts the RPEL motif and GAP
25 domain sequences. G-actin inhibits ArhGAP12 GAP activity, and this requires the G-actin
26 contacts identified in the structure. In melanoma cells, ArhGAP12 suppresses basal Rac and
27 Cdc42 activity, F-actin assembly, invadopodia formation, and experimental metastasis. In
28 B16 melanoma cells, ArhGAP12 mutants defective for G-actin binding exhibit more effective
29 downregulation of Rac.GTP loading following HGF stimulation, and enhanced Rac-
30 dependent processes, including invadopodia formation. Potentiation or disruption of G-
31 actin/ArhGAP12 interaction, by treatment with the actin-binding drugs latrunculin B or
32 cytochalasin D, has corresponding effects on Rac.GTP loading. G-actin interaction with
33 RPEL family rhoGAPs thus provides a negative feedback loop that couples Rac activity to
34 actin dynamics.

35

36 INTRODUCTION

37 Spatial and temporal control of the actin cytoskeleton in response to local signalling
38 or mechanical cues plays a critical role in development and disease¹⁻³. Underpinning it is the
39 regulation of actin treadmilling, the dynamic transition between actin's monomeric (G-actin)
40 and polymerised (F-actin) forms^{1,4}, which is controlled by rho family small GTPases^{5,6}. Rho
41 GTPase activity is potentiated by multiple rho GEF proteins, which catalyse GTP loading
42 and effector protein binding^{7,8}, and antagonised by inhibitory rho GAPs, which catalyse GTP
43 hydrolysis^{9,10}. Both are regulated by specific subcellular targeting, and by biological and
44 mechanical signals, but relatively little is known about how their activity responds to the
45 status of the actin cytoskeleton.

46 One connection between cytoskeletal dynamics and control of protein function is
47 provided by the RPEL proteins, which act as G-actin sensors^{11,12}. Their regulatory domains
48 contain RPEL motifs (Pfam PF02755), short polypeptide sequences that bind G-actin¹³. Two
49 RPEL protein families, the MRTFs and the Phactrs, have been characterised^{11,12,14,15}. The
50 MRTFs are coactivators for the SRF transcription factor, regulating expression of dozens of
51 cytoskeletal structural and regulatory proteins^{11,16,17}, while the Phactrs regulate cytoskeletal
52 dynamics by poorly understood mechanisms^{14,15,18,19}. G-actin controls the subcellular
53 localisation and activity of the MRTFs and Phactrs, at least in part by binding competitively
54 with their regulatory and effector proteins, such as importin $\alpha\beta$ and PP1, to sites within their
55 regulatory RPEL domains^{14,15,20,21}.

56 Here we identify two new RPEL protein families, the ArhGAP12 and ArhGAP32
57 subfamilies of Rac1/Cdc42-specific GTPase activating proteins (GAPs)²²⁻²⁵. The ArhGAP12
58 family is associated with actin-dependent cell surface structures and processes, including
59 adherens junctions^{23,26-28}, plasma membrane blebs²⁹, phagocytosis³⁰, and dendritic spines³¹,
60 while the ArhGAP32 family proteins have been implicated in protein trafficking and neuronal
61 development^{25,32}. However, little is known about their regulation. We show that binding of G-
62 actin to an atypical RPEL motif adjoining the ArhGAP12 GAP domain inhibits its GAP activity

63 for Rac1 *in vitro*. Disruption of the G-actin/ArhGAP12 interaction potentiates GAP activity *in*
64 *vivo*. Our findings demonstrate that G-actin/ArhGAP12 interaction constitutes a feedback
65 loop that couples Rac/Cdc42 GTP loading to the state of cytoskeletal dynamics.

66 RESULTS

67

68 **Two subfamilies of ArhGAP proteins contain a G-actin binding motif.**

69 The Starlet sea anemone *Nematostella vectensis* A7RG60 protein contains a single
70 canonical RPEL motif between its PH and GAP domains (<http://pfam.xfam.org/family/rpel>;
71 Fig. S1a,b). The A7RG60 RPEL-GAP region is closely related to two subfamilies of ArhGAP
72 proteins, ArhGAP9/12/15/27 and ArhGAP32/33, although the RPEL motif in these proteins
73 lacks the conserved RPEL glutamate residue (Fig. 1a,b; Fig. S1c,d). This residue does not
74 directly contact the bound actin, however, but contacts a second G-actin/RPEL unit in
75 proteins containing multiple RPEL motifs³³.

76 To test whether the ArhGAP non-consensus RPEL motif indeed binds G-actin, we
77 performed fluorescence anisotropy assays³⁴ (Fig. 1b, c). Peptides encompassing the
78 A7RG60, ArhGAP12- and ArhGAP32-family RPEL motifs bound G-actin with micromolar
79 affinities, comparable to those of the MRTFs and Phactrs^{13,14,34}, and binding was impaired to
80 varying extents by alanine substitution of the core RPEL arginine (Fig. 1c, Fig. S1e).
81 Biolayer interferometry analysis of a GST-RPEL^{ArhGAP12} fusion protein gave a comparable
82 result (2.85 μ M; Fig. S1f).

83

84 **Intact ArhGAP12 binds G-actin**

85 In MDCK epithelial cells, where ArhGAP12 promotes cell scattering²³, actin was
86 readily detectable in ArhGAP12 immunoprecipitates, and its recovery decreased following
87 serum stimulation, as seen with other RPEL proteins (Fig. 2a)^{11,14}. Similarly, ArhGAP12
88 coimmunoprecipitated with the non-polymerisable actin derivative R62D³⁵ upon transient
89 expression in NIH3T3 cells (Fig. 2b). ArhGAP12 did not colocalise with the F-actin
90 cytoskeleton in either cell type (Fig. S1g). Actin binding was not affected by deletion of the
91 SH3, WW or PH domain but was substantially reduced by the mutation or deletion of the

92 RPEL motif (Fig. 2b). Immobilised recombinant GST-ArhGAP12 and GST-ArhGAP32
93 derivatives could recover purified rabbit skeletal muscle LatB-actin from solution, provided
94 the RPEL motif was intact (Fig. 2c; Fig. S1h). Size exclusion chromatography of complexes
95 formed between LatB-actin and ArhGAP12 Δ N resolved an apparent 1:1 complex of M_r 90
96 kDa, whose formation was abolished by the R582A RPEL mutation (Fig. 2d); in contrast,
97 ArhGAP1, which does not contain an RPEL motif, did not bind actin in this assay (Fig. S1i).

98

99 **ArhGAP12/G-actin interaction involves both the RPEL motif and sequences within the**
100 **GAP domain.**

101 Using biolayer interferometry, we determined the affinity of LatB-actin for ArhGAP12
102 Δ N Δ P as 40.3 ± 1.5 nM (Fig. 3a). This is significantly greater than the ~micromolar affinity of
103 the G-actin/RPEL motif-peptide interaction, and suggests that G-actin might contact
104 additional sequences in the RPEL-GAP domain. To investigate interaction between G-actin
105 and ArhGAP12 in detail, we determined the structure of ArhGAP12 Δ N Δ P bound to LatB-
106 actin (hereafter ArhGAP12•G-actin) at a resolution of 2.6Å (Fig. 3b; Table 1). The
107 asymmetric unit contains four virtually identical copies of the complex, which superimpose
108 with RMSDs ranging from 0.18 Å to 0.35 Å (over 500 C α) (Fig. S2a). In the ArhGAP12•G-
109 actin complex, ArhGAP12 forms a striking U-shape, clasping G-actin with its RPEL motif and
110 GAP domain, which wrap around subdomains 1 and 3 (Fig. 3b). The extended
111 ArhGAP12/G-actin interaction surface (1700 Å²) includes close contacts between the RPEL
112 motif and the G-actin hydrophobic cleft and ledge (Fig. 3c, Fig. S2b), and between the GAP
113 domain and a hydrophobic niche at the subdomain 1/3 interface, composed of actin I75,
114 I175, and R177, and P109, L110, and P112 from the actin Pro-rich loop (Fig. 3d, Fig. S2c).

115 The ArhGAP12 RPEL motif interacts in a manner largely indistinguishable from that
116 seen in canonical RPEL motif•G-actin complexes^{13,33,36}, but makes two additional contacts
117 through T571 and F578 in helix α 1 (Fig. 3c, Fig. S2d). Alanine substitution of the conserved
118 RPEL motif core residue R582, or helix α 1 hydrophobic residues L575 and L579,

119 significantly reduced recovery of LatB-actin by ArhGAP12 Δ N Δ P in the pull-down assay
120 (Fig. 3e).

121 The GAP domain structure is essentially identical (RMSD 0.58 Å, 164 C α) to a
122 previously determined structure of the ArhGAP15 GAP domain (PDB 3BYI; Fig. S2e). The
123 aromatic sidechain of F650, from its helix α 5/ α 7 unit, is deeply buried in the hydrophobic
124 niche, while L642, A643 and M677 interact with the niche edges. These interactions are
125 further stabilised by a network of hydrogen bonds formed between N641, Q646, H654, E681
126 from the ArhGAP12 helix α 5/ α 7 unit and actin E72, L110, I175 and K113 respectively
127 (Figure 3d, Fig. S2c). Alanine- or charge-substitution of F650 reduced the recovery of G-
128 actin in the pulldown assay, with or without additional alanine substitutions at Q646 and
129 H654 (Fig. 3e). Biolayer interferometry analysis demonstrated that mutation of the GAP helix
130 α 5/ α 7 unit reduced binding affinity ~9-fold, while the RPEL R582A mutation reduced it 1300-
131 fold; binding of actin to a protein containing both mutations was undetectable (Fig. 3f; Fig.
132 S2f). Thus, the high binding affinity of G-actin for ArhGAP12 arises from contacts with both
133 the RPEL motif and GAP domain.

134

135 **G-actin inhibits ArhGAP12 GAP activity *in vitro***

136 We next investigated the effect of ArhGAP12/G-actin interaction on GAP activity. In a
137 colorimetric GAP assay measuring phosphate release, ArhGAP12 potentiated GTPase
138 activity of Rac1 and Cdc42, but not RhoA (Fig. S3a-c), in agreement with previous studies of
139 ArhGAP12/32 family members²²⁻²⁵, but it remains possible that other rho-family GTPases are
140 ArhGAP12 targets. GAP activity towards Rac1 was unaffected by the presence of
141 ArhGAP12 N-terminal sequences including the RPEL motif, or by RPEL point mutations that
142 reduce G-actin binding (Fig. 4a), but impaired by mutation of R637, the catalytic "arginine
143 finger" (Fig. 4a). Thus, in the absence of actin, the RPEL motif does not affect the *in vitro*
144 catalytic activity of ArhGAP12.

145 Inclusion of increasing concentrations of LatB-actin in the GAP reactions, however,
146 effectively inhibited ArhGAP12 GAP activity *in vitro* (Fig. 4b, Fig. S3d). Strikingly the RPEL
147 mutations R582A and L575A L579A, which reduce ArhGAP12/G-actin interaction, rendered
148 the GAP activity insensitive to inhibition by LatB-actin (Fig. 4b) as did mutations F650A and
149 F650D, which weaken the interaction between helix 5 of the GAP domain and the actin
150 hydrophobic niche (Fig. 4c). Thus, inhibition of ArhGAP12 GAP activity requires contact
151 between actin and both the GAP domain and the RPEL motif.

152

153 **G-actin partially occludes the GTPase binding site in the complex**

154 To understand further the molecular mechanism by which G-actin binding inhibits ArhGAP12
155 activity, we modelled the interaction of Rac and Cdc42 with ArhGAP12. Superposition of the
156 structure of the MgcRacGAP•Cdc42 complex GAP domain (PDB ID 5C2J) onto that of
157 ArhGAP12•G-actin (RMSD=0.63Å for 123 C α) revealed a substantial steric clash – 23.7%
158 of GTPase atoms – between G-actin and Cdc42, and superposition of the Rac1 structure
159 (PDB 5N6O) onto this model (RMSD 0.50Å for 148 C α), revealed a similar clash for Rac1
160 (23.5%; Fig. 4d, Fig. S3e). To test this we co-expressed ArhGAP12 derivatives with Rac^{G12V},
161 which is locked in the GTP-bound state, and assessed the ability of a GST-PAK CRIB
162 domain fusion protein to recover ArhGAP12 from cell lysates in association with Rac. RPEL
163 and GAP domain mutations that impair G-actin/ArhGAP12 interaction increased ArhGAP12
164 recovery in this assay (Fig. 4e). Taken together, these data suggest that GAP domain
165 interaction with the actin hydrophobic niche constrains its position so as to inhibit interaction
166 with its substrate GTPases.

167

168 **ArhGAP12 controls GTP loading on Rac and Cdc42 in melanoma cells**

169 ArhGAP15, an ArhGAP12 family member, is implicated in maintenance of basal
170 Rac.GTP levels in various cell types³⁷⁻³⁹. To investigate the role of ArhGAP12 in rho family

171 GTPase regulation we studied melanoma cells, whose behaviour in invasiveness and
172 experimental metastasis assays is Rac/Cdc42 dependent⁴⁰⁻⁴⁴. In B16F10 melanoma cells,
173 siRNA-mediated ArhGAP12 depletion did not appreciably affect transcription of other
174 ArhGAP12- and ArhGAP32-family members (Fig. S4a,b), but increased GTP loading on Rac
175 and Cdc42, (Fig. 5a,b), as did depletion of ArhGAP32 (Fig. S4c). We used the RaichuEV-
176 Rac FRET-based biosensor⁴⁵ to test how ArhGAP12 affects the kinetics of GTP loading on
177 Rac. In agreement with the pulldown experiments, the biosensor detected elevated basal
178 GTP loading on Rac in ArhGAP12-depleted cells (Fig. 5c); following stimulation by HGF,
179 downregulation was inhibited, taking at least twice as long to decrease to 50% of peak levels
180 (Fig. 5d,e; Fig. S4d). Thus, ArhGAP12 antagonises Rac and Cdc42 activity in B16F10
181 melanoma cells.

182

183 **ArhGAP12 controls invadopodia and experimental metastasis in melanoma cells**

184 Invadopodia are actin-rich membrane protrusions that degrade the extracellular
185 matrix to drive tumour cell invasion⁴⁶. Depletion of ArhGAP12 potentiated invadopodia
186 formation by B16F10 and B16F2 melanoma cells and their less invasive parent B16F0, and
187 by MDA-MB-231 mammary carcinoma cells (Fig. 6a; Fig. S4e,f); in B16F10 cells,
188 invadopodia formation was strongly dependent on Rac and to a lesser extent on Cdc42 (Fig.
189 6b). ArhGAP12 depletion also significantly increased the ability of B16F10 and B16F0 cells
190 to induce experimental metastasis in the mouse tail vein assay (Fig. 6c) without affecting cell
191 proliferation (Fig. S4g,h). Increased metastasis was strongly dependent on Rac (Fig. 6d) and
192 required MRTF/SRF signalling, as expected from our previous studies of B16F2 cells (Fig.
193 6d)⁴⁷. Consistent with this, ArhGAP12-depleted B16F10 cells exhibited a Rac-dependent
194 increase in F-actin (Fig. S5a,b), which was accompanied by increased nuclear accumulation
195 of MRTF-A and increased expression of MRTF/SRF target genes (Fig. S5c,d). ArhGAP12
196 also contributes to the maintenance of basal Rac activity in NIH3T3 fibroblasts, where it is
197 the only family member expressed (Fig. S5e): in resting cells, its depletion increased F-actin

198 levels, and promoted MRTF-A nuclear accumulation and MRTF/SRF target gene
199 expression¹¹ (Fig. S5f-i). ArhGAP12 therefore controls Rac-dependent processes in
200 melanoma and fibroblast cells.

201

202 **G-actin binding controls ArhGAP12 GAP activity *in vivo*.**

203 Finally we investigated the role of G-actin in ArhGAP12 regulation *in vivo*. B16F10-
204 derived cell lines conditionally expressing siRNA-resistant ArhGAP12 derivatives were
205 depleted of endogenous ArhGAP12, and their behaviour compared in the invadopodia and
206 metastasis assays. Re-expression of both wildtype and R582A ArhGAP12 effectively
207 suppressed the increased invadopodia formation, experimental metastasis, and F-actin
208 formation associated with ArhGAP12 depletion; the R582A mutant was more effective than
209 the wildtype protein at suppressing invadopodia formation, and was as effective as the
210 wildtype protein in the other assays, even though it was expressed at lower level (Fig. 7a,b,
211 Fig. S6a).

212 We used the depletion-rescue approach in conjunction with the RaichuEV-Rac FRET
213 biosensor to investigate the consequences of G-actin/ArhGAP12 interaction for Rac GTP
214 loading *in vivo*. B16F10 melanoma cells transiently expressing siRNA-resistant wildtype or
215 RPEL R582A mutant ArhGAP12 were depleted of endogenous ArhGAP12, and the kinetics
216 of Rac GTP loading following HGF stimulation measured. In this setting, expression of
217 ArhGAP12 R582A lowered the basal level of Rac-GTP loading more than wildtype
218 ArhGAP12, and altered the kinetics of Rac-GTP loading such that Rac downregulation
219 occurred more rapidly (Fig. 7c, Fig. S6b). Consistent with this, Rac.GTP pulldown assays
220 from B16F10 cells transiently expressing ArhGAP12 derivatives, together with myc-tagged
221 Rac, showed that Rac.GTP levels were lower in cells expressing the ArhGAP12 mutants
222 R582A and L575A L579A, which cannot bind G-actin, than in those expressing wildtype
223 ArhGAP12, even though the mutant proteins were less efficiently expressed (Fig. 7d).
224 Consistent with these results, expression of ArhGAP12 R582A in tetracycline-inducible

225 NIH3T3 cell lines decreased F-actin levels to a greater extent than wildtype ArhGAP12
226 (Fig. S6c,d).

227 The preceding results show that the RPEL motif exerts an inhibitory effect on
228 ArhGAP12 Rac GAP activity *in vivo*. To verify that this is a direct result of changes in
229 ArhGAP12/G-actin interaction, we examined the effects of actin-binding drugs on ArhGAP12
230 activity. Cytochalasin D (CD) and Latrunculin B (LatB) both bind G-actin, promoting F-actin
231 disassembly, but have opposing effects on RPEL proteins: CD binds G-actin competitively
232 with the RPEL motif and disrupts G-actin binding, while LatB is compatible with G-
233 actin/RPEL interaction^{11,12}. Accordingly, treatment of B16F10 cells with CD decreased Rac-
234 GTP level, whereas LatB treatment potentiated it, as assessed using the GST-PAK pulldown
235 assay (Fig. 7e). Strikingly, neither drug treatment affected Rac.GTP levels in ArhGAP12-
236 depleted cells, indicating that their effects require ArhGAP12 (Fig. 7f,g; Fig. S6e). Similar
237 results were obtained upon comparison of wildtype and ArhGAP12 knockout fibroblasts (Fig.
238 7h). Thus, G-actin controls cellular Rac GTP loading through its interaction with ArhGAP12-
239 family GAPs.

240

241 DISCUSSION

242 We have identified two new families of RPEL proteins, the ArhGAP12- and
243 ArhGAP32-family rhoGAPs, which contain a single atypical RPEL motif immediately N-
244 terminal to their GAP domains. G-actin forms a 1:1 complex with ArhGAP12, inhibiting its
245 GAP activity towards Rho and Cdc42. Actin makes canonical interactions with the RPEL
246 motif, and also interacts with the GAP domain through a hydrophobic 'niche' on its
247 subdomain 1/3 interface. Although the GAP domain contacts contribute only modestly to the
248 overall G-actin binding affinity, they are critical for the repressive effect of actin binding on
249 GAP activity. Inhibition of GAP activity by occlusion of the GTPase binding site is also seen
250 in the inhibitory interaction between DLC1 and the SH3 domain of p120RasGAP⁴⁸. Our
251 results show that G-actin binding to ArhGAP12 downregulates its GAP activity in melanoma
252 cells in vivo, sculpting the kinetics of Rac.GTP accumulation, and controlling Rac-dependent
253 processes such as invadopodia formation and experimental metastasis.

254 Extracellular chemical or environmental signals, and changes in cell differentiation
255 state are all associated with changes in actin dynamics. Since G-actin diffuses rapidly,
256 ArhGAP12/32-family members would effectively link the downstream functions of their target
257 GTPases, which include F-actin assembly, to the general state of actin cytoskeletal
258 dynamics, thereby constituting a feedback loop (Fig. 7i, left). ArhGAP12-family members are
259 also enriched at specific subcellular locations, such as epithelial cell junctions and
260 macrophage phagocytic cups^{23,30}. In such settings they could directly monitor local G-actin
261 fluctuations induced by their target GTPases, thereby fine-tuning GTPase activity, as part of
262 a local homeostatic feedback loop (Fig. 7i, right). Indeed, it has been proposed that
263 ArhGAP12 fulfils such a function at the phagocytic cup³⁰, and we are currently investigating
264 this further.

265 The ArhGAP12- and ArhGAP32-family rhoGAPs contain only a single atypical RPEL
266 motif lacking the conserved RPEL core glutamate (Pfam PF02755). Our previous studies of
267 multivalent G-actin/RPEL complexes showed that the glutamate contacts a second RPEL/G-

268 actin unit on its C-terminal side^{33,36}, and it is therefore unsurprising that atypical RPEL
269 motif peptides bind G-actin with comparable ~micromolar-range affinities^{13,14}. We estimated
270 the G-actin binding affinity of the intact ArhGAP12 RPEL-GAP fragment to be 40.3 ± 1.5 nM,
271 which is comparable to that estimated for the MRTF-A RPEL domain (~ 25 nM³⁵). We
272 therefore think it likely that the ArhGAPs and MRTFs will be similarly responsive to changes
273 in G-actin concentration, even though the ArhGAPs contain one rather than three RPEL
274 motifs. The development of sensors that allow tracking of G-actin concentration and
275 measurement of G-actin/RPEL interaction *in vivo* will be important to resolve this issue.

276 The actin hydrophobic niche identified here is conserved amongst different actin
277 family members, and it is therefore unlikely that different actins have differential effects on
278 ArhGAP12 activity. Although not previously implicated in interactions with other G-actin
279 binding proteins, the niche region mediates actin-actin interactions within the ADP F-actin
280 filament^{49,50}. In this context, however, it displays a more open conformation, with the
281 subdomain 1 Pro-rich loop interaction being disrupted to form the phosphate exit channel.
282 ADP-ribosylation of residue R177, at the niche edge, by bacterial toxins disrupts filament
283 formation (reviewed in ref⁵¹). The niche makes intimate contacts with the helix 5-7 unit of the
284 rhoGAP domain, just C-terminal to the catalytic arginine, which is implicated in GTPase
285 recognition¹⁰. ArhGAP12 F650, which docks in the niche, is conserved or substituted by
286 tyrosine or histidine in the other RPEL GAPs, but is generally hydrophilic in other rhoGAPs¹⁰
287 (Fig. S7). This, and the lack of RPEL motifs in other rhoGAPs, suggests that only the
288 ArhGAP12 and ArhGAP32 families are regulated by G-actin.

289 ArhGAP12 is present at high levels at adherens junctions, where it promotes cell-cell
290 adhesion^{23,26-28}, and at other actin-regulated cell surface structures such as plasma
291 membrane blebs, phagocytic cups and dendritic spines²⁹⁻³¹. Both ArhGAP12 and ArhGAP15
292 localisation is controlled by PI 3-kinase signalling^{30,39}, and the PH domain of the ArhGAP12
293 family member ArhGAP9 binds the phospholipid products of PI 3-kinase⁵². The PH domain
294 is just N-terminal to the RPEL motif, so we are currently investigating whether G-actin

295 binding also affects its function. The two ArhGAP32 family GAPs, contain an SH3 domain
296 N-terminal to the RPEL motif, and it will be interesting to see if G-actin influences its
297 interactions.

298 ArhGAP12 suppresses basal levels of GTP loading on Rac and Cdc42 in mouse
299 melanoma cells, as does the ArhGAP12 family protein ArhGAP15, in diverse settings,
300 including brain, glioma, 293 kidney cells and myeloid lineages³⁷⁻³⁹. This could occur in two
301 ways. First, depletion of ArhGAP12 from specific subcellular locations might increase
302 Rac.GTP at these locations, which could rapidly exchange with Rac pools elsewhere in the
303 cell. Alternatively, depletion of ubiquitously localised ArhGAP12 might impact global
304 Rac.GTP level directly, although one might expect such effects would be small given most
305 cells express multiple rho GAPs^{9,10}. Either way, depletion of ArhGAP12 in B16F10 cells
306 raises Rac GTP loading sufficiently to potentiate invadopodia formation and experimental
307 metastasis⁴⁰⁻⁴², the latter appearing to reflect Rac-dependent F-actin assembly and MRTF
308 activation. Interestingly, low ArhGAP12-family expression levels are associated with poor
309 survival in human melanoma in the TCGA database (see <http://www.oncolnc.org>).

310 We found that direct G-actin/ArhGAP12 interaction plays a significant role in control
311 of ArhGAP12 GAP activity. In melanoma cells, ArhGAP12 RPEL mutants defective in actin
312 binding exhibited greater GAP activity, were more effective at Rac downregulation following
313 growth factor stimulation, and in at least some biological assays, such as invadopodia
314 formation, were significantly more active than the wildtype protein. Moreover, the actin-
315 binding drugs CD and LatB had opposing effects on Rac GTP loading consistent with their
316 differential effects on G-actin/RPEL interaction, which were ArhGAP12-dependent.
317 Interestingly, in macrophages, which exhibit ArhGAP12-dependent phagocytosis, CD and
318 actin siRNA inhibit Rac and Cdc42 activation, and LPS-stimulated phagocytosis^{30,53}, while in
319 neutrophils, LatB treatment prevents ArhGAP15-dependent Rac down-regulation following
320 PI3K activation³⁹. Our findings suggest that these observations reflect the direct control of
321 ArhGAP12 family proteins by G-actin in these contexts.

322 The RPEL motif present in the ArhGAP12 and ArhGAP32 proteins couples their
323 activity to the surrounding availability of G-actin (Fig. 7i). We therefore consider it likely that
324 these rhoGAPs will be involved in biological processes that are critically reliant on local
325 control of F-actin assembly. Our future work will focus on elucidating how ArhGAP12 family
326 members' activity relates to fluctuations in local G-actin concentration.

327 ACKNOWLEDGEMENTS

328 We thank the Crick Science Technology platforms for support and advice during this work,
329 especially Matthew Renshaw and Kurt Anderson (Advanced Light Microscopy), Probir
330 Chakravarty and Aengus Stewart (Bioinformatics and Biostatistics), Clare Watkins and Julie
331 Bee (Biological Resources), Namita Patel and Alireza Alidoust (Fermentation Facility), Derek
332 Davis (Flow Cytometry), Graham Clark (Genomics Equipment Park), Mike Howell
333 (Highthroughput screening), Nicola O'Reilly (Peptide Chemistry), and Phil Walker (Structural
334 biology). X-ray data were collected at the Diamond Light Source (ID24 beamline, mx8015).
335 We thank Michiyuki Matsuda (Kyoto University) for the RaichuEV-Rac plasmid, and Michael
336 Way and members of the RT and NM groups for helpful discussions. This work was
337 supported by Cancer Research UK core funding until March 31st 2015. Since then support
338 to RT and NQM has been by the Francis Crick Institute, which receives its core funding from
339 Cancer Research UK (FC001-190, FC001-115), the UK Medical Research Council (FC001-
340 190, FC001-115) and the Wellcome Trust (FC001-190, FC001-115); and by ERC Advanced
341 Grant 268690 to RT.

342

343 AUTHOR CONTRIBUTIONS

344 All authors designed and interpreted experiments. JD conducted biochemical and cell
345 biological studies; SM determined the structure of the actin/ArhGAP12 complex and
346 conducted comparative structural analysis. JD and RT wrote the manuscript with input from
347 SM and NQM.

348

349 DATA AVAILABILITY

350 The ArhGAP12/G-actin structure has been deposited in the Protein Data Bank
351 (www.pdb.org) with the primary accession code 6GVC. Structures of MRTF-A RPEL2/G-
352 actin and ArhGAP15 that were re-analysed in this study were obtained from PDB under the
353 accession codes 2V52 and 3BYI respectively. Source data for Fig. 1c, Fig. 2a,d, Fig. 3a,f,

354 Fig. 4a,b,c, Fig. 5a,b,c,d, Fig. 6a,b,c,d, Fig. 7a,b,c,e,f,h and Supplementary Fig. S1e,f,i,
355 Fig. S2f, Fig. S3c,d, Fig. S4b,c,d,f,g,h, Fig. S5a,b,c,d,g,h,i, Fig. S6a,b,c,e have been
356 provided as Supplementary Table 1. All other data supporting the findings of this study are
357 available from the corresponding author upon request.

358

359 **COMPETING FINANCIAL INTERESTS**

360 The authors declare no competing financial interests.

361

362

363 **REFERENCES**

364

- 365 1. Krause, M. & Gautreau, A. Steering cell migration: lamellipodium dynamics and the
366 regulation of directional persistence. *Nat Rev Mol Cell Biol* **15**, 577-590 (2014).
- 367 2. Przybyla, L., Muncie, J.M. & Weaver, V.M. Mechanical Control of Epithelial-to-
368 Mesenchymal Transitions in Development and Cancer. *Annu Rev Cell Dev Biol* **32**,
369 527-554 (2016).
- 370 3. Skau, C.T. & Waterman, C.M. Specification of Architecture and Function of Actin
371 Structures by Actin Nucleation Factors. *Annu Rev Biophys* **44**, 285-310 (2015).
- 372 4. Dominguez, R. & Holmes, K.C. Actin structure and function. *Annu Rev Biophys* **40**,
373 169-186 (2011).
- 374 5. Lawson, C.D. & Ridley, A.J. Rho GTPase signaling complexes in cell migration and
375 invasion. *J Cell Biol* **217**, 447-457 (2018).
- 376 6. Hodge, R.G. & Ridley, A.J. Regulating Rho GTPases and their regulators. *Nat Rev*
377 *Mol Cell Biol* **17**, 496-510 (2016).
- 378 7. Cook, D.R., Rossman, K.L. & Der, C.J. Rho guanine nucleotide exchange factors:
379 regulators of Rho GTPase activity in development and disease. *Oncogene* **33**, 4021-
380 4035 (2014).
- 381 8. Laurin, M. & Cote, J.F. Insights into the biological functions of Dock family guanine
382 nucleotide exchange factors. *Genes & development* **28**, 533-547 (2014).
- 383 9. Tcherkezian, J. & Lamarche-Vane, N. Current knowledge of the large RhoGAP
384 family of proteins. *Biol Cell* **99**, 67-86 (2007).
- 385 10. Amin, E. *et al.* Deciphering the Molecular and Functional Basis of RHOGAP Family
386 Proteins: A systematic approach toward selective inactivation of rho family proteins. *J*
387 *Biol Chem* **291**, 20353-20371 (2016).
- 388 11. Miralles, F., Posern, G., Zaromytidou, A.I. & Treisman, R. Actin dynamics control
389 SRF activity by regulation of its coactivator MAL. *Cell* **113**, 329-342 (2003).

- 390 12. Vartiainen, M.K., Guettler, S., Larijani, B. & Treisman, R. Nuclear actin regulates
391 dynamic subcellular localization and activity of the SRF cofactor MAL. *Science* **316**,
392 1749-1752 (2007).
- 393 13. Mouilleron, S., Guettler, S., Langer, C.A., Treisman, R. & McDonald, N.Q. Molecular
394 basis for G-actin binding to RPEL motifs from the serum response factor coactivator
395 MAL. *The EMBO journal* **27**, 3198-3208 (2008).
- 396 14. Wiezlak, M. *et al.* G-actin regulates the shuttling and PP1 binding of the RPEL
397 protein Phactr1 to control actomyosin assembly. *Journal of cell science* **125**, 5860-
398 5872 (2012).
- 399 15. Huet, G. *et al.* Actin-regulated feedback loop based on Phactr4, PP1 and cofilin
400 maintains the actin monomer pool. *Journal of cell science* **126**, 497-507 (2013).
- 401 16. Esnault, C. *et al.* Rho-actin signaling to the MRTF coactivators dominates the
402 immediate transcriptional response to serum in fibroblasts. *Genes & development* **28**,
403 943-958 (2014).
- 404 17. Cen, B. *et al.* Megakaryoblastic leukemia 1, a potent transcriptional coactivator for
405 serum response factor (SRF), is required for serum induction of SRF target genes.
406 *Molecular and cellular biology* **23**, 6597-6608. (2003).
- 407 18. Allen, P.B., Greenfield, A.T., Svenningsson, P., Haspeslagh, D.C. & Greengard, P.
408 Phactrs 1-4: A family of protein phosphatase 1 and actin regulatory proteins. *Proc*
409 *Natl Acad Sci U S A* **101**, 7187-7192 (2004).
- 410 19. Sagara, J. *et al.* Scapinin, a putative protein phosphatase-1 regulatory subunit
411 associated with the nuclear nonchromatin structure. *J Biol Chem* **278**, 45611-45619
412 (2003).
- 413 20. Pawłowski, R., Eeva Kaisa Rajakylä, E.K., Vartiainen, M.K. & Treisman, R. An actin-
414 regulated importin α/β -dependent extended bipartite NLS directs nuclear import of
415 MRTF-A. *The EMBO journal* **29**, 3448-3458 (2010).

- 416 21. Hirano, H. & Matsuura, Y. Sensing actin dynamics: structural basis for G-actin-
417 sensitive nuclear import of MAL. *Biochem Biophys Res Commun* **414**, 373-378
418 (2011).
- 419 22. Furukawa, Y. *et al.* Isolation of a novel human gene, ARHGAP9, encoding a rho-
420 GTPase activating protein. *Biochem Biophys Res Commun* **284**, 643-649 (2001).
- 421 23. Gentile, A. *et al.* Met-driven invasive growth involves transcriptional regulation of
422 Arhgap12. *Oncogene* **27**, 5590-5598 (2008).
- 423 24. Seoh, M.L., Ng, C.H., Yong, J., Lim, L. & Leung, T. ArhGAP15, a novel human
424 RacGAP protein with GTPase binding property. *FEBS Lett* **539**, 131-137 (2003).
- 425 25. Zhao, C. *et al.* GC-GAP, a Rho family GTPase-activating protein that interacts with
426 signaling adapters Gab1 and Gab2. *J Biol Chem* **278**, 34641-34653 (2003).
- 427 26. Matsuda, M. *et al.* Identification of adherens junction-associated GTPase activating
428 proteins by the fluorescence localization-based expression cloning. *Exp Cell Res*
429 **314**, 939-949 (2008).
- 430 27. Monastyrskaya, K. *et al.* miR-199a-5p regulates urothelial permeability and may play
431 a role in bladder pain syndrome. *Am J Pathol* **182**, 431-448 (2013).
- 432 28. Rudnicki, A. *et al.* Next-generation sequencing of small RNAs from inner ear sensory
433 epithelium identifies microRNAs and defines regulatory pathways. *BMC Genomics*
434 **15**, 484 (2014).
- 435 29. Lecat, S., Matthes, H.W., Pepperkok, R., Simpson, J.C. & Galzi, J.L. A Fluorescent
436 Live Imaging Screening Assay Based on Translocation Criteria Identifies Novel
437 Cytoplasmic Proteins Implicated in G Protein-coupled Receptor Signaling Pathways.
438 *Mol Cell Proteomics* **14**, 1385-1399 (2015).
- 439 30. Schlam, D. *et al.* Phosphoinositide 3-kinase enables phagocytosis of large particles
440 by terminating actin assembly through Rac/Cdc42 GTPase-activating proteins. *Nat*
441 *Commun* **6**, 8623 (2015).
- 442 31. Ba, W. *et al.* ARHGAP12 Functions as a Developmental Brake on Excitatory
443 Synapse Function. *Cell Rep* **14**, 1355-1368 (2016).

- 444 32. Nakamura, T. *et al.* PX-RICS mediates ER-to-Golgi transport of the N-
445 cadherin/beta-catenin complex. *Genes Dev* **22**, 1244-1256 (2008).
- 446 33. Mouilleron, S., Wiezlak, M., O'Reilly, N., Treisman, R. & McDonald, N.Q. Structures
447 of the Phactr1 RPEL domain and RPEL motif complexes with G-actin reveal the
448 molecular basis for actin binding cooperativity. *Structure* **20**, 1960-1970 (2012).
- 449 34. Guettler, S., Vartiainen, M.K., Miralles, F., Larijani, B. & Treisman, R. RPEL motifs
450 link the serum response factor cofactor MAL but not myocardin to Rho signaling via
451 actin binding. *Molecular and cellular biology* **28**, 732-742 (2008).
- 452 35. Posern, G., Sotiropoulos, A. & Treisman, R. Mutant actins demonstrate a role for
453 unpolymerized actin in control of transcription by serum response factor. *Mol Biol*
454 *Cell* **13**, 4167-4178 (2002).
- 455 36. Mouilleron, S., Langer, C.A., Guettler, S., McDonald, N.Q. & Treisman, R. Structure
456 of a pentavalent G-actin*MRTF-A complex reveals how G-actin controls
457 nucleocytoplasmic shuttling of a transcriptional coactivator. *Sci Signal* **4**, ra40 (2011).
- 458 37. Radu, M. *et al.* ArhGAP15, a Rac-specific GTPase-activating protein, plays a dual
459 role in inhibiting small GTPase signaling. *J Biol Chem* **288**, 21117-21125 (2013).
- 460 38. Zamboni, V. *et al.* Disruption of ArhGAP15 results in hyperactive Rac1, affects the
461 architecture and function of hippocampal inhibitory neurons and causes cognitive
462 deficits. *Sci Rep* **6**, 34877 (2016).
- 463 39. Graziano, B.R. *et al.* A module for Rac temporal signal integration revealed with
464 optogenetics. *J Cell Biol* **216**, 2515-2531 (2017).
- 465 40. Kurisu, S., Suetsugu, S., Yamazaki, D., Yamaguchi, H. & Takenawa, T. Rac-WAVE2
466 signaling is involved in the invasive and metastatic phenotypes of murine melanoma
467 cells. *Oncogene* **24**, 1309-1319 (2005).
- 468 41. Nakahara, H. *et al.* Involvement of Cdc42 and Rac small G proteins in invadopodia
469 formation of RPMI7951 cells. *Genes Cells* **8**, 1019-1027 (2003).

- 470 42. Yamaguchi, H. *et al.* Sphingosine-1-phosphate receptor subtype-specific positive
471 and negative regulation of Rac and haematogenous metastasis of melanoma cells.
472 *Biochem J* **374**, 715-722 (2003).
- 473 43. Stengel, K. & Zheng, Y. Cdc42 in oncogenic transformation, invasion, and
474 tumorigenesis. *Cell Signal* **23**, 1415-1423 (2011).
- 475 44. Revach, O.Y., Winograd-Katz, S.E., Samuels, Y. & Geiger, B. The involvement of
476 mutant Rac1 in the formation of invadopodia in cultured melanoma cells. *Exp Cell*
477 *Res* **343**, 82-88 (2016).
- 478 45. Komatsu, N. *et al.* Development of an optimized backbone of FRET biosensors for
479 kinases and GTPases. *Mol Biol Cell* **22**, 4647-4656 (2011).
- 480 46. Eddy, R.J., Weidmann, M.D., Sharma, V.P. & Condeelis, J.S. Tumor Cell
481 Invadopodia: Invasive Protrusions that Orchestrate Metastasis. *Trends Cell Biol* **27**,
482 595-607 (2017).
- 483 47. Medjkane, S., Perez-Sanchez, C., Gaggioli, C., Sahai, E. & Treisman, R. Myocardin-
484 related transcription factors and SRF are required for cytoskeletal dynamics and
485 experimental metastasis. *Nat Cell Biol* **11**, 257-268 (2009).
- 486 48. Jaiswal, M. *et al.* Functional cross-talk between ras and rho pathways: a Ras-specific
487 GTPase-activating protein (p120RasGAP) competitively inhibits the RhoGAP activity
488 of deleted in liver cancer (DLC) tumor suppressor by masking the catalytic arginine
489 finger. *J Biol Chem* **289**, 6839-6849 (2014).
- 490 49. Fujii, T., Iwane, A.H., Yanagida, T. & Namba, K. Direct visualization of secondary
491 structures of F-actin by electron cryomicroscopy. *Nature* **467**, 724-728 (2010).
- 492 50. Murakami, K. *et al.* Structural basis for actin assembly, activation of ATP hydrolysis,
493 and delayed phosphate release. *Cell* **143**, 275-287 (2010).
- 494 51. Aktories, K., Lang, A.E., Schwan, C. & Mannherz, H.G. Actin as target for
495 modification by bacterial protein toxins. *FEBS J* **278**, 4526-4543 (2011).
- 496 52. Ceccarelli, D.F. *et al.* Non-canonical interaction of phosphoinositides with pleckstrin
497 homology domains of Tiam1 and ArhGAP9. *J Biol Chem* **282**, 13864-13874 (2007).

- 498 53. Kong, L. & Ge, B.X. MyD88-independent activation of a novel actin-Cdc42/Rac
499 pathway is required for Toll-like receptor-stimulated phagocytosis. *Cell Res* **18**, 745-
500 755 (2008).
501
502

503 **FIGURE LEGENDS**

504

505 **Figure 1 Two families of rhoGAPs contain an RPEL motif.** See also Fig. S1 and
506 Supplementary Table 1. **(a)** Domain structure of ArhGAP12 and ArhGAP32 rhoGAP
507 subfamilies. The RPEL-like motif is indicated in red. **(b)** Clustal X sequence alignment of the
508 RPEL-like motifs of ArhGAP12/32 family GAPs with the RPEL motif of *Nematostella*
509 *vectensis* A7RG60, aligned with the Pfam PF02755 HMM logo. **(c)** Fluorescence anisotropy
510 analysis of LatB-actin binding to the FAM-conjugated RPEL peptides shown in **(b)**, or
511 derivatives in which the core RPEL arginine is replaced by alanine. Data were fitted by non-
512 linear regression; data are means \pm SEM, $n=6$. ND, not determined.

513

514 **Figure 2 ArhGAP12 interaction with G-actin requires the RPEL motif.** See also Fig. S1,
515 S8 and Supplementary Table 1. **(a)** Endogenous ArhGAP12 was immunoprecipitated and
516 actin recovery was analysed by immunoblot in starved MDCK cells. Cells were transfected
517 with control or ArhGAP12 siRNA, or serum-stimulated as indicated. Data are mean \pm SEM,
518 $n=4$ experiments, two-tailed unpaired t-test. **(b)** Top, ArhGAP12 derivatives: full-length (FL),
519 amino acids 1-791; Δ N 410-791; Δ N Δ P 568-791; Δ N Δ P Δ R, 582-791. RPEL point mutants
520 were R582A and L575A L579A. Bottom, nonpolymerisable actin mutant R62D was
521 coexpressed with wildtype ArhGAP12 or RPEL mutant R582A and their interaction analysed
522 by immunoprecipitation and immunoblotting. **(c)** Immobilised recombinant GST-ArhGAP12
523 proteins were used to recover purified LatB-actin from solution; actin recovery was analysed
524 by immunoblot. **(d)** Analytical gel filtration. Elution profiles of recombinant ArhGAP12 Δ N (4
525 μ M) and purified LatB-actin (5 μ M) either alone (solid lines) or in a mixture (dotted lines),
526 analysed by absorbance (top) or SDS-PAGE/Coomassie blue staining (bottom). Apparent
527 Mr are indicated. Black and open horizontal arrowheads point to ArhGAP12 and actin
528 respectively. Data shown in **(a)** and **(b-d)** are representative of $n=4$ and 3 experiments
529 respectively.

530

531 **Figure 3 Structural analysis of the ArhGAP12•G-actin complex.** See also Fig. S2, S8
532 and Supplementary Table 1. (a) Octet biolayer interferometry assay. Biosensors loaded with
533 GST-ArhGAP12 Δ N Δ P were incubated with different concentrations of G-actin, which was
534 washed out at 400s. K_d is the mean \pm SEM; a representative of 3 independent experiments
535 is shown. (b) The ArhGAP12 Δ N Δ P•LatB-actin complex. ArhGAP12 Δ N Δ P is shown as blue
536 ribbon, and LatB-actin in white surface representation, with subdomains indicated and the
537 hydrophobic cleft, ledge and niche surfaces coloured in blue, pink and yellow, respectively.
538 The GAP domain catalytic arginine finger is indicated. (c) RPEL-actin interactions. RPEL
539 residues interacting with actin are shown as sticks; RPEL sequence, secondary structures,
540 and interacting residues (mutated residues highlighted) are summarised below. (d) GAP
541 domain interactions with the actin hydrophobic niche. ArhGAP12 residues interacting with
542 the actin niche, or stabilising the orientation of the helices, are shown as sticks. GAP domain
543 helix interaction residues and secondary structures are summarised as in (c), with asterisks
544 indicating residues implicated in interaction with rho-family GTPases¹⁰ (catalytic arginine
545 finger R637 in red). (e) Effect of RPEL and GAP domain mutations on G-actin binding,
546 assessed by pulldown assay as in Fig. 2c and detected by Coomassie blue staining. LatB-
547 actin recovery, quantified relative to GST-ArhGAP12 Δ N WT, is indicated below the gels.
548 Black and open arrowheads point to ArhGAP12 and actin respectively. Representative data
549 of $n=3$ experiments. (f) Summary of Octet biolayer interferometry assays for GST-ArhGAP12
550 Δ N Δ P and its mutant derivatives, and GST-RPEL. K_d is the mean \pm SEM, n as indicated;
551 n.d., no binding detectable under the assay conditions.

552

553 **Figure 4 G-actin inhibits ArhGAP12 GAP activity by occluding rho protein binding.**
554 See also Fig. S3, S8 and Supplementary Table 1. GAP activity towards Rac1 was assessed
555 using a colorimetric assay for P_i release. Data were fitted by non-linear regression; data are
556 means \pm SEM, $n=3$ (a left, b), $n=4$ (a right, c). (a) Effect of ArhGAP12 truncations and point

557 mutations of the RPEL motif or catalytic R637. (b) GAP activity is suppressed by 10 μ M
558 LatB-actin, and this requires the RPEL motif. (c) Alanine or aspartate substitutions at niche
559 contact residue F650 do not affect GAP activity, but relieve the inhibitory effect of LatB-actin.
560 (d) Model of Rac1 bound to ArhGAP12. The GAP domain of the MgcRacGAP:Cdc42.GDP
561 structure (PDB ID 5C2J) was superimposed onto the GAP domain of the ArhGAP12
562 Δ N Δ P \bullet actin structure. The Rac1 structure (PDB 5N6O) was then superimposed onto the
563 Cdc42 model (RMSD 0.50 \AA , 148 C α). Exposed and occluded Rac1 residues are shown as
564 green and red ribbons, GDP in orange. The degree of occlusion is similar for Cdc42 (23.7%)
565 and Rac1 (23.5%). (e) Flag-ArhGAP12 derivatives and constitutively active Myc-Rac^{G12V}
566 were co-expressed in NIH 3T3 cells; and recovery of ArhGAP12 and Myc-Rac^{G12V} in GST-
567 PAK CRIB pulldown assays assessed by immunoblotting. Representative immunoblots from
568 3 independent experiments are shown.

569

570 **Figure 5 ArhGAP12 controls GTP loading on Rac and Cdc42 in melanoma cells.** See
571 also Fig. S4, S5, S8 and Supplementary Table 1. B16F10 melanoma cells were transfected
572 with control or ArhGAP12 siRNA. (a) Rac.GTP and (b) Cdc42.GTP levels, as assessed by
573 GST-PAK pulldown assays. Left, representative immunoblots. Right, data summary. Data
574 are means \pm SEM, $n=6$ (a) or $n=3$ (b), two-tailed unpaired t-test. (c) Increased basal Rac
575 GTP loading in serum-starved B16F10 cells, measured using the RaichuEV-Rac FRET
576 biosensor. FRET/CFP ratio was measured over 9 min in control ($n=22$) or ArhGAP12-
577 depleted ($n=32$) cells. Data are means \pm SEM, two-tailed Mann Whitney test. (d) Kinetics of
578 Rac GTP loading in control ($n=10$) and ArhGAP12-depleted ($n=9$) B16F10 cells following
579 HGF stimulation, measured as in (c). Data are expressed relative to control cell value at the
580 start of the experiment. T_{50} , time to recover to 50% peak Rac GTP loading. Data are means
581 \pm SEM. (e) Representative FRET/CFP ratio images displayed in 8-color, intensity modulated
582 display mode. Representative images of three independent experiments. Scale bar 20 μ m.

583

584 **Figure 6 ArhGAP12 regulates Rac-dependent processes in cells.** See also Fig. S4,
585 S5, S8. Cells were transfected with control, ArhGAP12 or other siRNA as indicated. **(a,b)**
586 Invadopodia formation by cells plated overnight on Oregon-green labelled gelatin was
587 detected by loss of staining. **(a)** At least 8,507 cells, 112 images per condition from $n=16$
588 wells. **(b)** At least 30,675 cells, 96 images per condition from $n=24$ wells. Data points from
589 three experiments were combined; data are means \pm SEM, two-tailed Mann Whitney test.
590 **(c,d)** Experimental metastasis assay. B16F0 and F10 cells were injected in the tail vein of
591 C57BL/6J mice. Images show lung colonisation after 12 days. Box-and-whiskers plots
592 indicate the number of lung metastases, showing median, quartiles, and highest and lowest
593 values. Representative results of three experiments are shown; $n=5$ **(c)** and $n=10$ **(d)** mice
594 per group, except B16F10/siArhGAP12 for which $n=4$ **(c)** and $n=8$ **(d)**, two-tailed Mann
595 Whitney test.

596

597 **Figure 7 G-actin regulates Rac activity in melanoma cells.** See also Fig. S5, S6, S8 and
598 Supplementary Table 1. **(a,b)** B16F10 conditional lines expressing control or siRNA-resistant
599 Flag-ArhGAP12 derivatives were transfected with control or ArhGAP12 siRNA. **(a)**
600 Invadopodia formation assessed as in Fig. 6b. At least 22,437 cells, 96 images per condition
601 from $n=24$ wells. Data points from three experiments were combined; data are means \pm
602 SEM, two-tailed Mann Whitney test. **(b)** Experimental metastasis assay, displayed as in Fig.
603 6d. Representative results of three experiments are shown, $n=5$ mice per group, two-tailed
604 Mann Whitney test. **(c)** HGF-induced Rac.GTP loading imaged using the RaichuEV-Rac
605 biosensor. siRNA-resistant Flag-ArhGAP12 WT or R582A were transiently re-expressed in
606 serum-starved ArhGAP12-depleted B16F10 cells. Images were acquired from control
607 ($n=96$), +ArhGAP12 WT ($n=58$) and +ArhGAP12 R582A ($n=37$) cells. (i) Basal GTP loading
608 on Rac, measured by FRET/CFP ratio over 10 min before stimulation. Data are means \pm
609 SEM, two-tailed Mann Whitney test. Note the lower expression level of ArhGAP12 R582A.
610 (ii) Kinetics of GTP loading on Rac following HGF stimulation, normalised taking the basal

611 activity in control cells as 1.0. Data are means \pm SEM. **(d)** Immunoblot analysis of GST-
612 PAK Rac pulldown assays using lysates of B16F10 cells cotransfected with Flag-ArhGAP12
613 derivatives and Myc-Rac. Representative immunoblot from one of three independent
614 experiments. **(e)** B16F10 cells, maintained in 0.3% FCS, following treatment with
615 Cytochalasin D (CD) or Latrunculin B (LatB) for 30 min before Rac.GTP pulldown assay.
616 Data are means \pm SEM $n=3$, two-tailed unpaired t test. **(f)** Cells transfected with control or
617 ArhGAP12 siRNA were maintained in 10% FCS and treated with CD for 30 min before
618 Rac.GTP pulldown assays. Data are means \pm SEM, $n=5$ (control), $n=11$ (siArhGAP12) two-
619 tailed unpaired t test. **(g)** Cells as in (f) were treated with LatB for 30 min before Rac.GTP
620 pulldown assay. A representative immunoblot of three independent experiments is shown.
621 **(h)** Wildtype and ArhGAP12 knockout MEFs were treated with LatB for 30 min, and with
622 PDGF for 5 min before Rac.GTP pulldown assay. Data are means \pm SEM, $n=5$ (WT), $n=3$
623 (KO), two-tailed unpaired t test. **(i)** Global and local regulation by RPEL rhoGAP proteins.

624

625 **Table 1** Crystallographic data collection and structure refinement statistics.

626

627

1 METHODS

2

3 **Plasmids.** ArhGAP12 cDNA (short isoform encoding a 791 amino acid-protein, Uniprot
4 S4R248) was amplified by PCR from an NIH 3T3 cDNA library using standard techniques.
5 ArhGAP12 derivatives were expressed in mammalian cells with N-terminal Flag tag in pEF-
6 plink¹¹ or pcDNA4TO (Invitrogen) or as N-terminal GFP fusion in pcDNA6.2-N-EmGFP
7 (Invitrogen), and in bacteria as GST fusion in pGex-6P-2 vector. Point mutants and siRNA-
8 oligonucleotide 11-resistant ArhGAP12 derivatives were generated by site-directed
9 mutagenesis (three mismatches: 5'-GAG CAT GTC-3' to 5'-GAA CAC GTI-3')(Quikchange,
10 Agilent). Deletion mutants were created using the Phusion high-fidelity protocol (New
11 England Biolabs). For lentiviral transduction, Flag-ArhGAP12 sequences were cloned into a
12 modified pTripz vector (Dharmacon), where RFP and microRNA regulation sequences were
13 replaced by a bGH Poly(A) sequence using In-fusion HD cloning (Takara). The ArhGAP32
14 RPEL-GAP domain (amino-acids 339-569) was expressed in bacteria as GST fusion using a
15 pGex-6P-2 vector. Expression plasmids for Actin R62D and Rac have been described³⁵. All
16 plasmids were sequenced using Sanger sequencing.

17

18 **Protein expression, purification and size-exclusion chromatography.** Rabbit skeletal
19 muscle LatB-actin was prepared as described³⁴. ArhGAP12 and ArhGAP32 protein
20 expression was induced at 37°C in *Escherichia coli* Rosetta (DE3) pLysS. Bacteria were
21 harvested by centrifugation and lysed in 20 mM Tris, pH 6.8 and 8.5 respectively, 150 mM
22 NaCl, 10 mM MgCl₂, 1% Triton X-100, 1 mM DTT, 1 mM phenylmethylsulphonyl fluoride and
23 protease inhibitors (Roche). The GST-fusion proteins were adsorbed onto a glutathione-
24 sepharose resin (GE Healthcare), and ArhGAP12 derivatives were recovered by cleavage
25 with 3C protease overnight at 4°C in 20 mM Tris pH 6.8, 150 mM NaCl, 10 mM MgCl₂, 1 mM
26 DTT. Proteins were then purified by size exclusion chromatography using a Superdex 200

27 column (GE Healthcare) in 50 mM Tris, pH 6.8, 150 mM NaCl, 10 mM MgCl₂, 1 mM DTT.
28 The purity of the proteins was examined by SDS-PAGE and Coomassie brilliant blue
29 staining (Fig. S3b).

30

31 **Analytical size exclusion chromatography and *in vitro* pulldown assays.** For gel
32 filtration analyses, 4 μM of purified ArhGAP12 derivatives or recombinant GST-ArhGAP1
33 (Cytoskeleton, GAS01) were incubated with 5 μM or 2 μM LatB-actin respectively and
34 loaded on a calibrated Superdex 200 (10:300) column (GE Healthcare) in 50 mM Tris, pH
35 6.8 and 7.6 respectively, 150 mM NaCl, 10 mM MgCl₂, 1 mM DTT. Fractions collected were
36 concentrated, and a tenth of each fraction was analysed by SDS-PAGE and Coomassie
37 brilliant blue staining. For GST pulldown experiments, glutathione-sepharose beads (GE
38 Healthcare) were saturated with GST-ArhGAP12 or GST-ArhGAP32 from *E. coli* lysates,
39 and used as an affinity resin in a binding reaction with 10 μM LatB-actin in binding buffer (50
40 mM Tris, pH 7.0 and pH 8.5 respectively, 50 mM NaCl, 5 mM MgCl₂) for 1h at 4°C. The resin
41 was then washed 4 times in binding buffer and subjected to SDS-PAGE, Coomassie staining
42 or Western blotting. Coomassie brilliant blue staining was performed according to standard
43 techniques, and quantified using Image Studio after scanning with an Odyssey infrared
44 scanner (Licor). Actin recovery was quantified relative to input GST-ArhGAP12.
45 Unprocessed scans of blots and Coomassie gels are shown in Supplementary Figure 8.

46

47 **Crystallisation, data collection and refinement of the ArhGAP12•G-actin complex.** The
48 protein complex was prepared by mixing purified ArhGAP12 ΔNΔP and LatB-actin in a 1:2
49 molar ratio and further purified by Superdex 200 size-exclusion chromatography equilibrated
50 in 20 mM Tris, pH 8, 50 mM NaCl, 3 mM MgCl₂, 0.2 mM EGTA, 0.2 mM ATP and 0.3 mM
51 TCEP. To grow crystals, the protein solution was concentrated to 30 mg/mL. The complex
52 was crystallised at 20°C using the sitting-drop vapour diffusion method. Drops of 0.5 μL

53 consisted of a 1:1 (vol:vol) mixture of protein and a well solution containing 0.1 M Bis-Tris
54 Propane, pH 6.5, 20% PEG 3350, 0.2 M sodium thiocyanate. Crystals appeared after five
55 days and reached their maximum size after ten days. Crystals were cryoprotected in mother
56 liquor supplemented with 20% glycerol and then flash-frozen in liquid nitrogen. X-ray data
57 were collected at 100 K at the ID24 beamline (mx8015) of the Diamond Light Source
58 synchrotron (DLS, Oxford, United Kingdom). Data collection and refinement statistics are
59 summarised in Table 1. The data set was indexed, scaled and merged using xia2⁵⁴.
60 Molecular replacement was achieved by using the high resolution atomic coordinates of G-
61 actin extracted from the RPEL2•LatB-actin¹³ structure (PDB ID 2V52) and the GAP domain
62 extracted from ArhGAP15 structure (PDB ID 3BYI) in PHASER⁵⁵. Refinement was carried
63 out by using Phenix⁵⁶. Model building was carried out in COOT⁵⁷. Model validation used
64 PROCHECK⁵⁸, and figures were prepared using the graphics program PYMOL 2.1.1⁵⁹. The
65 asymmetric unit contains 4 copies of the complex. The ArhGAP12•G-actin structure has
66 been deposited in PDB (ID 6GVC).

67

68 **Protein affinity measurements.** Fluorescence anisotropy assays were performed as
69 described previously³⁴. Dissociation constants were derived by nonlinear regression analysis
70 of the data using Prism (GraphPad software). Biolayer interferometry analysis of G-actin
71 binding to immobilised GST-ArhGAP12 was performed using the Octet Red96 (ForteBio);
72 typical immobilisation levels were above 2.5 nm. GST-ArhGAP12 loaded anti-GST
73 biosensors were incubated with various concentrations of G-actin in the kinetics buffer (25
74 mM Tris pH7.5, 100 mM NaCl, 0.1% Tween 20, 5 mM MgCl₂, 0.5 mM TCEP, 1 mg/mL BSA).
75 Binding experiments were performed in solid-black 96-well plates, at 25°C with an agitation
76 speed of 1,000 rpm. Data analysis was done using the Octet software version 7.1 (ForteBio).
77 Global fitting of the binding curves generated a best fit with a 1:1 model and the kinetic
78 association and dissociation constants were calculated. The quality of the fit was assessed

79 by evaluation of the χ^2 and R^2 values generated from all the fitting analyses. Experiments
80 were repeated at least 3 times.

81

82 **RhoGTPase activity assays.** GAP activity was measured using a colorimetric rhoGAP
83 assay kit (Cytoskeleton, BK105). The reactions were performed in 20 μ L with 4.75 μ M
84 RhoGTPase, 2 μ M ArhGAP12 derivatives (Fig. S3b), in presence or absence of 10 μ M LatB-
85 actin, at 37°C for the indicated time after addition of 200 μ M GTP. The release of inorganic
86 phosphate (P_i) was detected at 650 nm using a SpectraMax Plus 384-well plate reader. A
87 KH_2PO_4 solution was used to calibrate the quantity of P_i (nmol) released to the absorbance.
88 A non-linear regression analysis was applied to the data using Prism (GraphPad software).

89

90 **Cell lines.** B16F0, B16F2, B16F10 melanoma cells, SV40 immortalised MEFs, NIH3T3
91 fibroblasts, MDCK II epithelial cells and MDA-MB-231 breast carcinoma cells were
92 maintained in DMEM with 10% fetal calf serum (FCS). Where indicated, cells were serum
93 starved (0.3% FCS) overnight, then treated for 30 min with 15% FCS, 100 ng/mL HGF
94 (Millipore, GF414), 5 μ M Cytochalasin D (Merck, 250255), or 1 μ M Latrunculin B (Merck,
95 428020). NIH 3T3 monoclonal lines stably expressing Flag-tagged ArhGAP12 derivatives
96 and the Tet repressor were generated using pcDNA4TO-Flag-ArhGAP12 and pcDNA6/TR
97 (Invitrogen) plasmids, and selected for zeocin (200 μ g/mL) and blasticidin (5 μ g/mL)
98 resistance. Expression was induced overnight with 2 μ g/mL Tetracycline. B16F10 polyclonal
99 lines conditionally expressing Flag-ArhGAP12 derivatives were generated by lentiviral
100 transduction using pTripz-Flag-ArhGAP12 plasmids, and selected for puromycin (0.5 μ g/mL)
101 resistance. Expression was induced for 24h with 2 μ g/mL Doxycycline. Cell growth was
102 analysed following seeding and siRNA transfection of 50,000 cells in a well of a 6-well plate.
103 Each day, cells of replicate wells were trypsinised, resuspended in media and counted using
104 the Countess II instrument (Invitrogen). For cell cycle analysis cells were fixed after 2.5h of
105 BrdU incorporation, counterstained with Propidium iodide, and analysed by flow cytometry

106 using standard methods and FlowJo software as previously described⁴⁷. All cell lines tested
107 negative for mycoplasma and were authenticated by STR profiling by Crick Cell Services.

108

109 **Transfection, immunoblotting and immunofluorescence.** Cells were transfected with
110 expression plasmids using Lipofectamine 2000 according to the manufacturer's protocol
111 (Invitrogen, 11668-019). Cells were reverse transfected with RNAi oligonucleotides using
112 Lipofectamine RNAiMax (Invitrogen, 13778-150). siRNAs were: control
113 UUCUCCGAACGUGUCACGU; MRTF-A/B UGGAGCUGGUGGAGAAGAA; ArhGAP32:
114 L057176-01; Rac1: L041170-00; Cdc42: L043087-01; ArhGAP12: mouse L-040581-01 (a
115 pool of oligonucleotides J-040581-9, -10, -11 and -12) and human L-008729-01 Dharmacon
116 smartpools. In experiments where siRNA-resistant ArhGAP12 derivatives were re-
117 expressed, either transiently or in ArhGAP12-expressing lines, ArhGAP12 siRNA
118 oligonucleotide 11 (GCAUUGAGCAUGUCGAAGA) was used. In MDCK II cells, the
119 oligonucleotide targeting ArhGAP12 was GAACAGAACUGCUAAUUCAUU. Assays were
120 performed 72h after siRNA transfection, with the exception of the experimental metastasis
121 assay (40h); where required, siRNA-depleted cells were transfected with ArhGAP12
122 plasmids 24h before analysis.

123 Whole cell extract preparation and immunoblotting were performed using standard
124 techniques. Unprocessed scans of blots are shown in Fig. S8. For phenotypic experiments,
125 samples were taken for analysis of protein expression at the time assays were commenced.
126 Antibodies used were against β -actin (Santa-Cruz Biotechnology, clone C4, sc47778,
127 1:1,000 dilution), HA (Roche, 3F10, 11867431001, 1:1,000 dilution), Rac (Millipore, clone
128 23A8, 05-389, 1:500 dilution), Cdc42 (Millipore, 05-542, 1:250 dilution), MRTF-A (Santa-
129 Cruz Biotechnology, C-19, sc21558, 1:1,000 dilution), MRTF-B (Bethyl Laboratories, A302-
130 768, 1:1,000 dilution), Myc (Crick Biological Resources Facilities, clone 9E10, 1:1,000
131 dilution), ArhGAP12 (Sigma, HPA000412, 1:1,000 dilution), α -Tubulin (Sigma, clone B5-1-2,
132 T5168, 1:6,000 dilution), GST (Sigma, G7781, 1:10,000 dilution) and Flag (Sigma, F7425,

133 1:1,000 dilution). Secondary antibodies were IRDye-680LT or -800CW conjugated (Licor,
134 925-68022, -68023, -32212, -32214, -32219, 1:10,000 dilution). For coimmunoprecipitation
135 experiments in MDCK cells, Alexa Fluor 790 conjugated light chain specific IgG (Jackson
136 Immunoresearch laboratories, 211-652-171 and 115-655-174, 1:5,000 dilution) were used.
137 Immunoblots were scanned with an Odyssey infrared scanner (Licor) and quantified using
138 Image Studio. Immunofluorescence assays were carried out as described previously¹¹. F-
139 actin was detected with Alexa Fluor 647- or Texas Red-Phalloidin (Invitrogen, A22287 and
140 T7471) and DNA was counterstained using DAPI. F-actin staining was imaged in 96-well
141 glass bottom plates on the automated Cellomics Arrayscan VTi and the intensity was
142 measured using the Target Activation Bioapplication (Cellomics). Where indicated, cells
143 were imaged using a confocal Laser Scanning Microscope LSM710 controlled by the Zen
144 software (Zeiss), with a 63x/1.40 oil Plan Apochromat objective lens (Zeiss), utilising the 405
145 (DAPI), 488 (GFP) and 561 nm (Texas-Red) lasers for excitation, and a pinhole set at 1 Airy
146 unit.

147

148 **Immunoprecipitation and Rac/Cdc42 pulldown experiments.** For Flag
149 immunoprecipitation, cells were lysed in IP buffer (50 mM Tris, pH 7.8, 100 mM NaCl, 1%
150 Triton X-100, 1 mM DTT and protease inhibitors (Roche)). The soluble fraction was
151 precleared with Protein A-Sepharose beads (Sigma), and incubated with M2-Agarose beads
152 (2h, 4°C, Sigma) with rotation. ArhGAP12 immunoprecipitation was performed with
153 essentially the same protocol with the exception that it used 50 mM NaCl, Dynabeads
154 Protein G (Invitrogen) and a pan-ArhGAP12 polyclonal antibody generated by Crick
155 Biological Resources Facilities. Beads were washed four times in IP buffer and resuspended
156 in SDS Laemmli buffer. Actin recovery was quantified relative to input. Rac/Cdc42 pulldown
157 experiments were performed using 15 µL of GST-tagged human PAK1 p21-binding domain
158 (residues 67-150, 1 µg/µL) bound to glutathione magnetic beads (Millipore, 17-10394),

159 carried out according to the manufacturer's instructions. Rac/Cdc42 GTP loading was
160 quantified relative to total Rac/Cdc42. ArhGAP12 recovery was quantified relative to input.
161

162 **Gene expression.** Total RNA was isolated and cDNA was synthesised as described
163 previously¹⁶. Amounts of cDNA corresponding to 10 ng of RNA were analysed in SYBR
164 Green based real-time quantitative PCR (Invitrogen) using ABI Prism 7900HT and
165 QuantStudio 5 detection systems (Applied Biosystems). Absolute quantification of cDNA
166 abundance was determined using a mouse genomic DNA standard. Data were normalised
167 to the abundance of *Gapdh* cDNA. Gene-specific exonic primers were as follows:

168 *Arhgap9* (CAGAGGGCACTGACCAGAAGA and TTGGCGATTAGCCGCTTTAA),
169 *Arhgap12* (ACAACCCAGGAGCGAACCT and TCGGCTTGTGCTCACATCTC),
170 *Arhgap15* (CTACAGGAGCTGTGCAAATGAGA and TTGGCTCTGCCTGTCTTGGT),
171 *Arhgap27* (GAGGCCTGAAAGCGACTT and GGGTCGTCTCTGTAGGAATTTACG),
172 *Arhgap32* (CACCGCCTCCGAAAAATG and TGCAGACTCAGCTAACGCTAGTG),
173 *Arhgap33* (TGGCGATGATCTGGATTTCA and AAGTCAAGTCCCCGAAGTCCTT),
174 *Srf* (GGTTGGAGGGAACCACTGT and CTGGGAGAAGGGGGAAGAC),
175 *Cyr61* (AATCGCAATTGAAAAGGCA and TGAAAAGAACTCGCGGTTTCG),
176 *Vcl* (AGCCCAGATGCTTCAGTCAGA and GGTCAGATGTGCCAGAAAGGA),
177 *Gapdh* (TCTTGTGCAGTGCCAGCCT and CAATACGGCCAAATCCGTTCA).

178 Intronic primers were as follows:

179 *Cyr61* (CGTAAACTGCCCTGAGCCTA and GACGCGATCGAGACACTTCT),
180 *Klf7* (CACTGGCTCCCTATACCGTG and GATCCAAAGCAGGGTTTGCC),
181 *Slc2a1* (CCGGATTTACGGAACCCCTC and GCAAAGGCGGGACAAGAAAG),
182 *Srf* (TCAAGGCAGCAGCAGTTTCT and CAGGCAGGGTTAGGAACCAAG),
183 *Vcl* (CGTCACTTGC GTTGAGTACC and GAAACCACCCACAGGTTGGA),
184 *Zyx* (CAACCTGGCTCGTTCTCACT and GACCATAACGAGGGGCTCAG).

185 **Time-lapse FRET imaging.** Cells were transiently transfected with the RaichuEV-Rac
186 FRET biosensor⁴⁵, 24h before imaging. Cells were imaged in phenol-red free DMEM using
187 an inverted microscope with Perfect Focus System (Nikon Ti2), controlled by the Micro-
188 Manager software⁶⁰, with a 60x/1.4 NA Plan Apochromat objective lens (Nikon), an ASI XY
189 stage with piezo Z, a scientific CMOS camera (Photometrics Prime), a SpectraX LED light
190 engine (Lumencor) utilising the blue excitation light fitted with a 440/20 nm filter, an
191 FF459/526/596-Di01 dichroic mirror (Semrock), and two emission filters (FF01-482/25 for
192 CFP, FF01-544/24 for YFP). After background subtraction, FRET/CFP ratio images were
193 generated using Metamorph (Molecular Devices) and represented in the intensity modulated
194 display mode (8 colours). CFP and FRET intensities were averaged over the whole cell area
195 using Fiji software⁶¹. For kinetics experiments, data were expressed relative to the start of
196 the experiment, and normalised as indicated. The determination of t_{50} (time to downregulate
197 to 50% of the maximum activity) for each condition is calculated using the formula: $t_{50} = t(\text{Min}$
198 $+ 50\% (\text{Max} - \text{Min})) - t(\text{Max})$ where t represents time, Min the minimum value, Max the
199 maximum value (Fig. S4d, S6b).

200

201 **Invadopodia assay.** Invadopodia assays were carried out in 96-well glass bottom plates,
202 coated with Poly-D-Lysine (50 $\mu\text{g}/\text{mL}$), functionalised with 0.5% glutaraldehyde, and coated
203 for 30 min at 37°C with 33 $\mu\text{g}/\text{mL}$ Oregon Green-Gelatin (Invitrogen, G13186) and 1%
204 unlabelled gelatin in PBS. Cells (3000 per well) were seeded and incubated for 16h, fixed
205 with 4% PFA, and stained for F-actin and DNA. Images were captured on the Cellomics
206 Arrayscan VTi with a 5x objective and analysed using the automated Morphology Explorer
207 Bioapplication (Cellomics). Quantitation was by loss of fluorescence, normalised to cell
208 number.

209

210 **Animals and experimental metastasis assay.** The experimental metastasis assays were
211 performed as described previously⁴⁷. B16F0 (900,000 cells) and B16F10 cells (200,000 or

212 500,000 cells) were injected into the tail vein of 7-week old C57BL/6J females, and lungs
213 were analysed 12 days after injection by counting surface metastatic foci macroscopically.
214 For phenotypic rescue experiments, mice were given water supplemented with 2 mg/mL
215 Doxycycline and 1% sucrose two days prior to injection and for the duration of the
216 experiment, and replaced every two days. ArhGAP12 knockout embryos were obtained from
217 the Jackson Laboratories, and knockout MEFs were generated and genotyped using
218 standard techniques. Animal experimentation complied with all ethical regulations and was
219 carried out under the UK Home Office Project licence P7C307997 in the Crick Biological
220 Resources Facilities.

221

222 **Multiple sequence alignment and phylogenetic tree.** The protein sequences of all mouse
223 rhoGAP domains and fifty amino acids N-terminally were taken from the RefSeq database. A
224 multiple sequence alignment was generated using default parameters in Clustal Omega, and
225 used to produce a phylogenetic tree by the neighbour-joining method. The alignment was
226 edited and Clustal X-coloured in Jalview (blue, hydrophobic; red, positively charged;
227 magenta, negatively charged; green, polar; pink, cysteine; orange, glycine; yellow, proline;
228 cyan, aromatic; white, unconserved). The cladogram was drawn using Dendroscope.

229

230 **Statistics and reproducibility.** Each experiment was performed at least three times.
231 Unless indicated otherwise, nonparametric two-tailed Mann-Whitney tests were used to
232 determine statistical significance, where * $P < 0.05$, ** $P < 0.01$, *** $P < 0.001$, **** $P <$
233 0.0001 ; ns, not significant. Error bars represent SEM for n independent experiments, as
234 indicated in the legends. Statistical analyses were performed using Prism (GraphPad
235 software).

236 REFERENCES

237

238 54. Winter, G., Lobley, C.M. & Prince, S.M. Decision making in xia2. *Acta Crystallogr D*
239 *Biol Crystallogr* **69**, 1260-1273 (2013).

240 55. McCoy, A.J. *et al.* Phaser crystallographic software. *J Appl Crystallogr* **40**, 658-674
241 (2007).

242 56. Adams, P.D. *et al.* PHENIX: a comprehensive Python-based system for
243 macromolecular structure solution. *Acta Crystallogr D Biol Crystallogr* **66**, 213-221
244 (2010).

245 57. Emsley, P., Lohkamp, B., Scott, W.G. & Cowtan, K. Features and development of
246 Coot. *Acta Crystallogr D Biol Crystallogr* **66**, 486-501 (2010).

247 58. Vaguine, A.A., Richelle, J. & Wodak, S.J. SFCHECK: a unified set of procedures for
248 evaluating the quality of macromolecular structure-factor data and their agreement
249 with the atomic model. *Acta Crystallogr D Biol Crystallogr* **55**, 191-205 (1999).

250 59. Schrodinger, L. (2010).

251 60. Edelstein, A.D. *et al.* Advanced methods of microscope control using muManager
252 software. *J Biol Methods* **1** (2014).

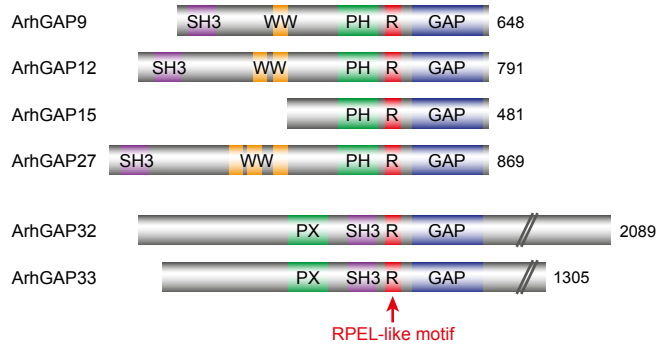
253 61. Schindelin, J. *et al.* Fiji: an open-source platform for biological-image analysis.
254 *Nature methods* **9**, 676-682 (2012).

255

256

FIGURE 1

a



b



c

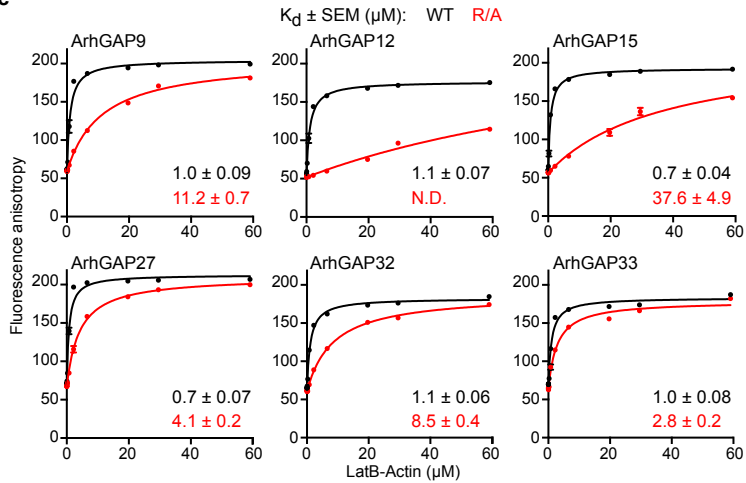
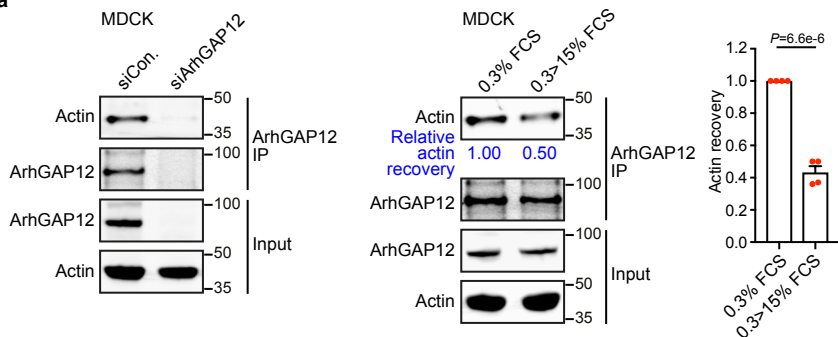
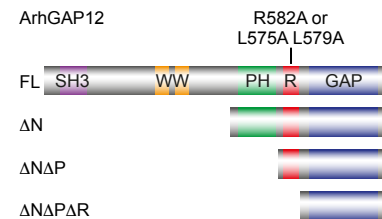


FIGURE 2

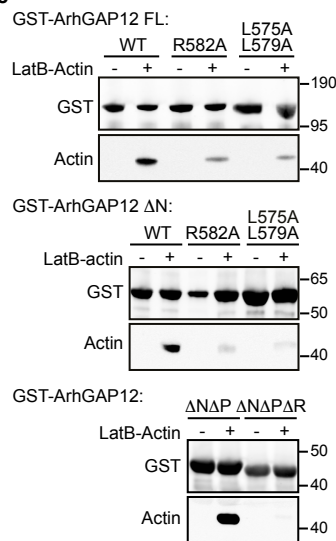
a



b



c



d

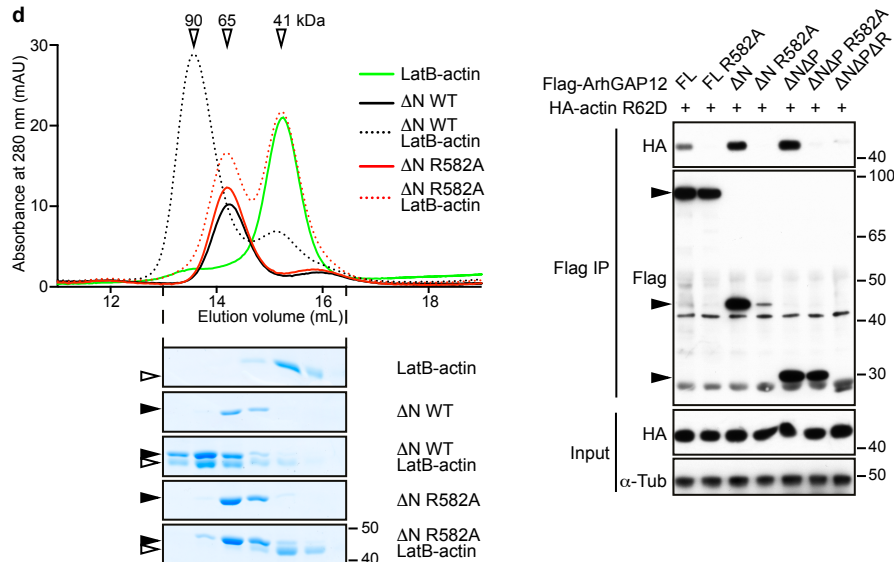
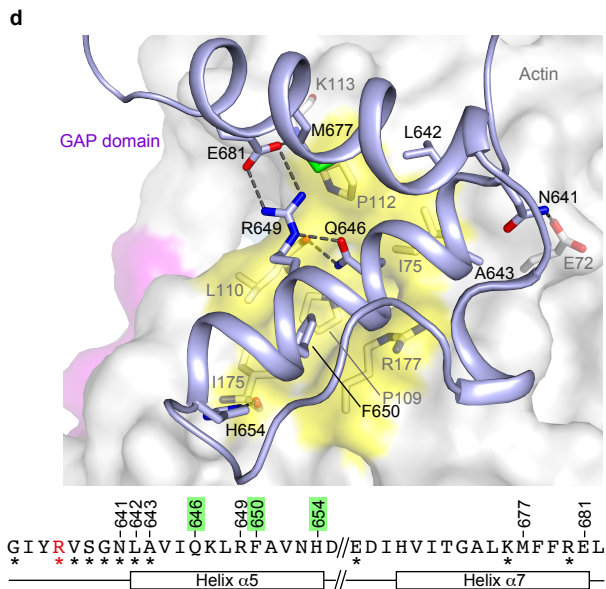
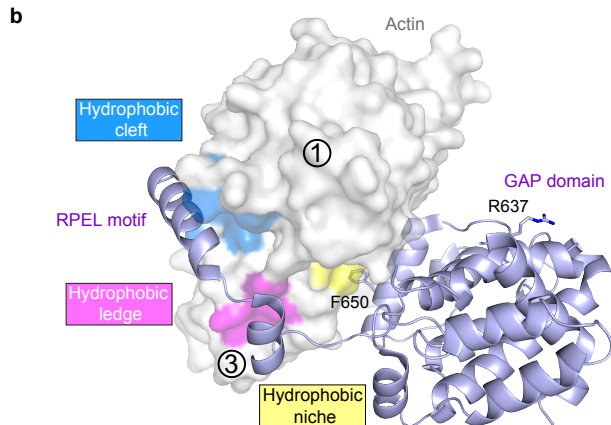
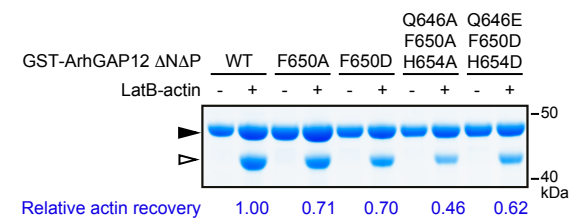
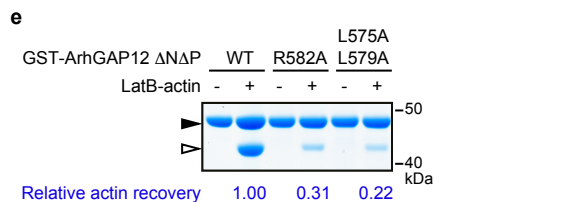
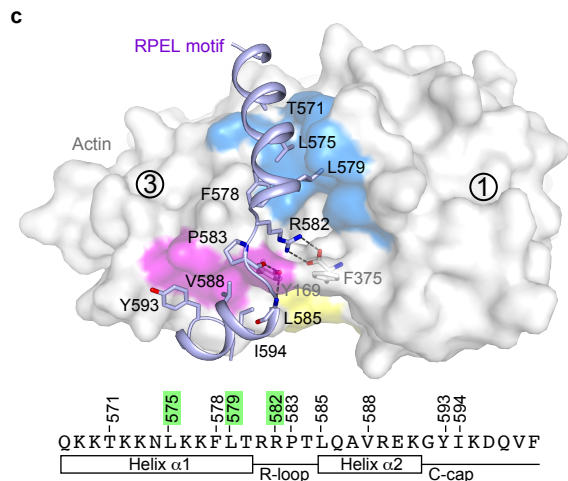
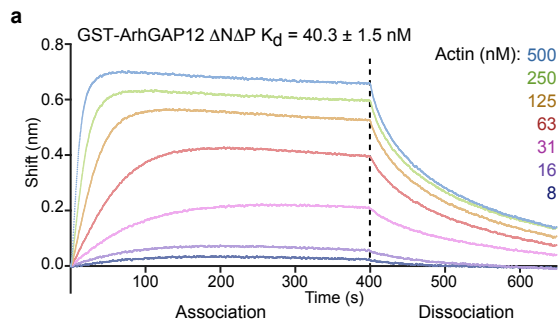


FIGURE 3

f

GST-ArhGAP12:	Mean $K_d \pm$ SEM (μM)	n
WT	0.040 ± 0.001	3
$\Delta\text{N}\Delta\text{P}$ R582A	52.2 ± 2.4	5
Q646A F650A H654A	0.359 ± 0.005	8
R582A Q646A F650A H654A	n.d.	3
RPEL	2.85 ± 0.09	6

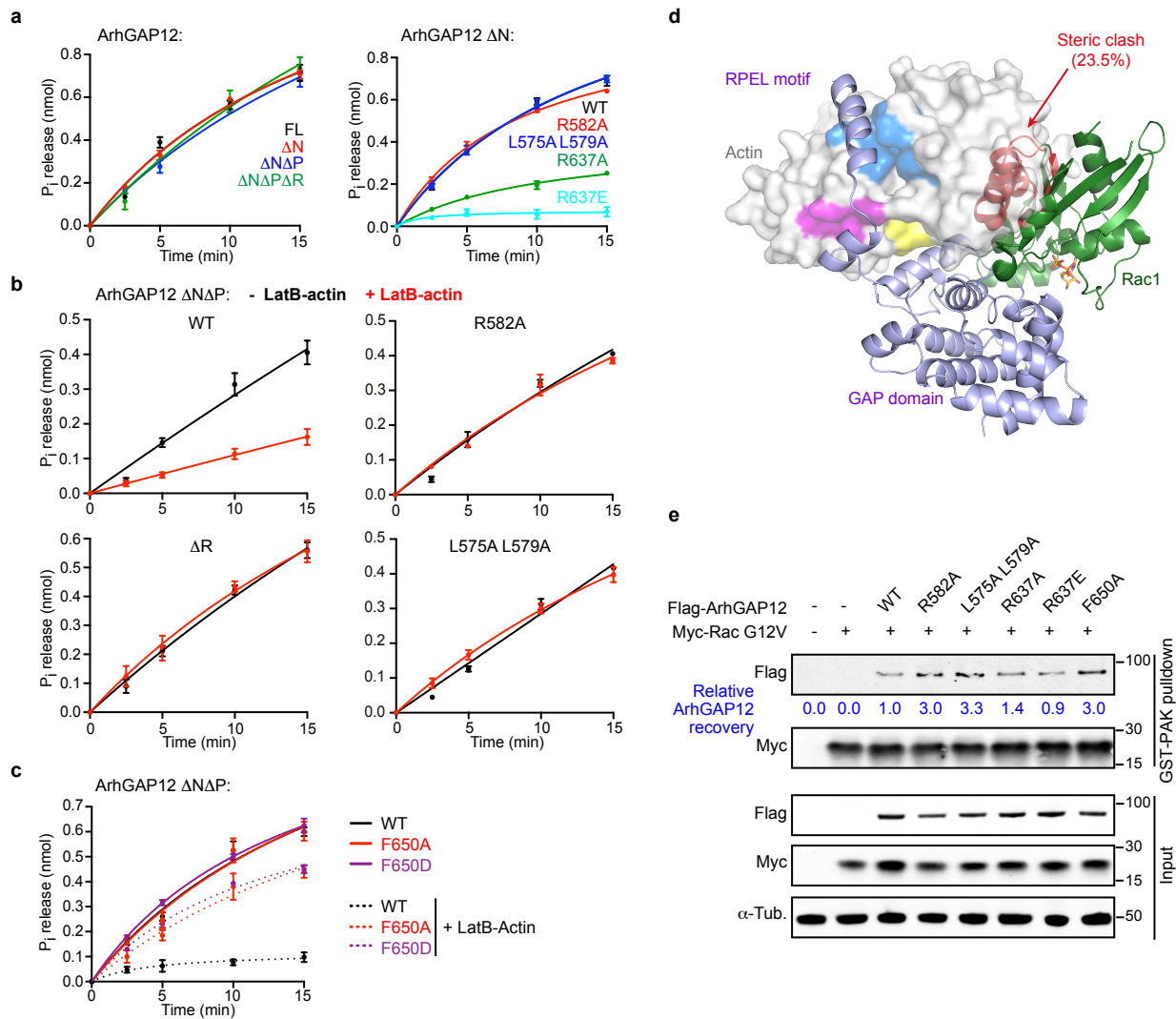
FIGURE 4

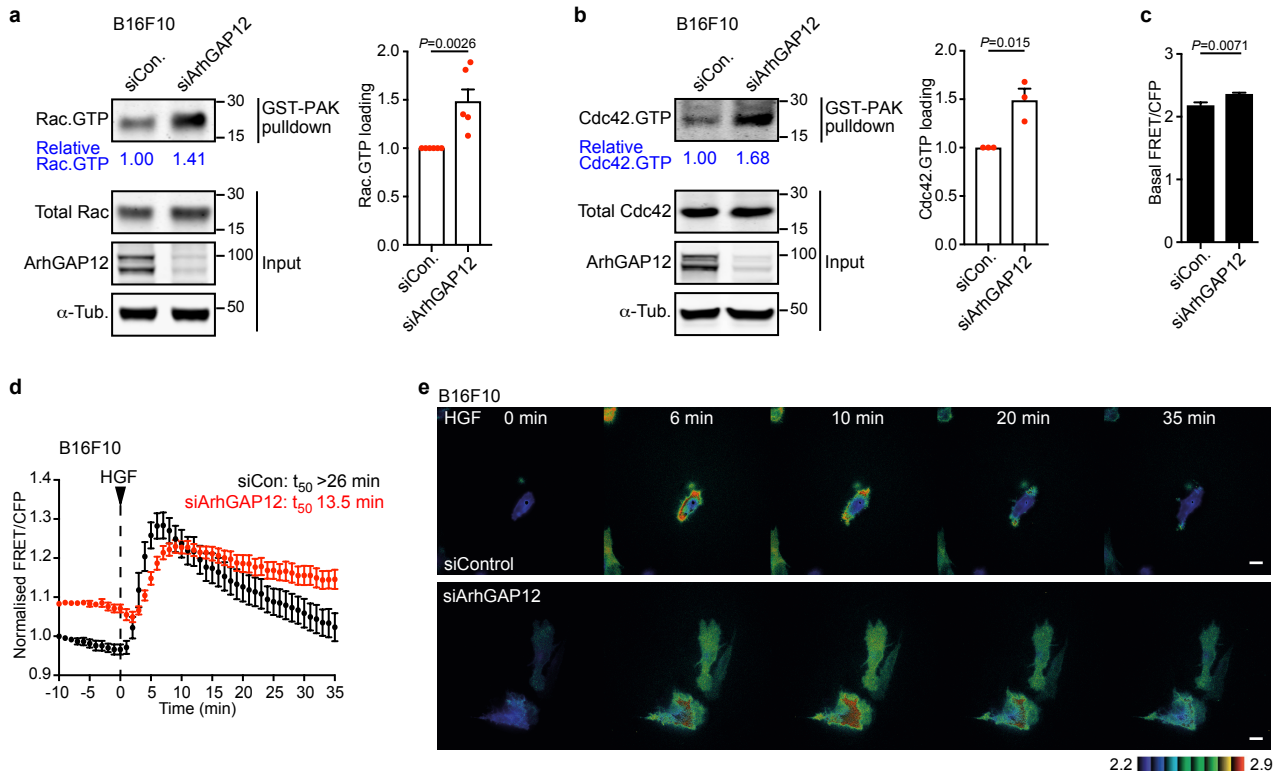
FIGURE 5

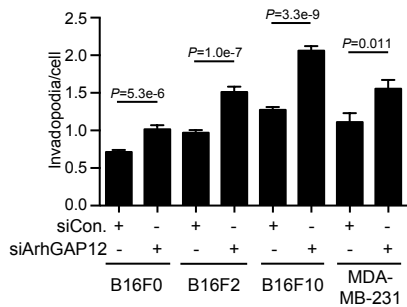
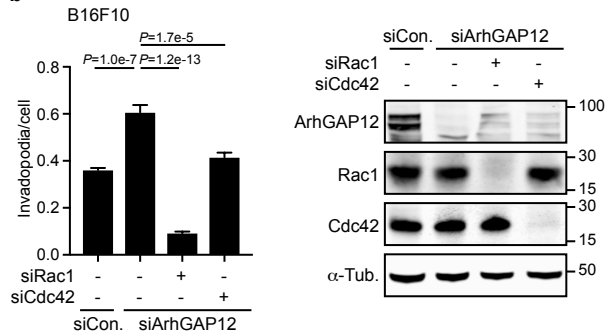
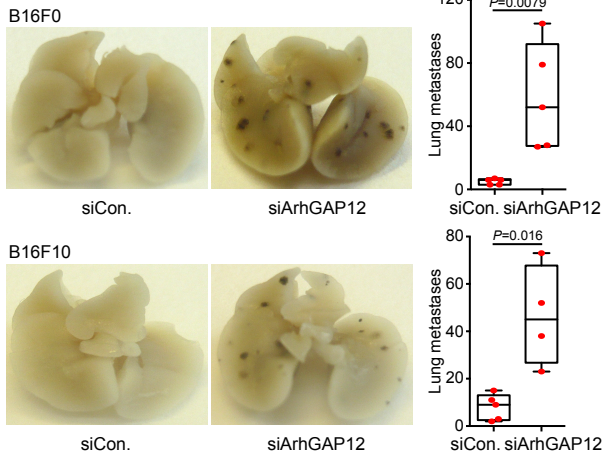
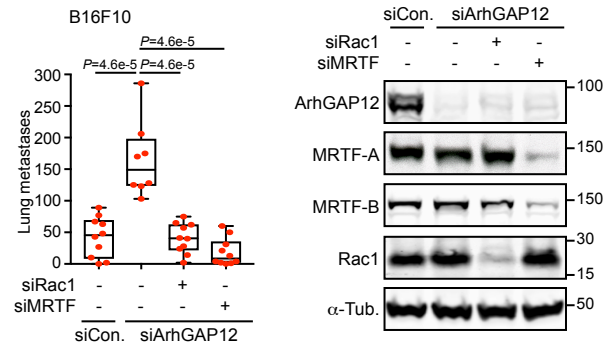
FIGURE 6**a****b****c****d**

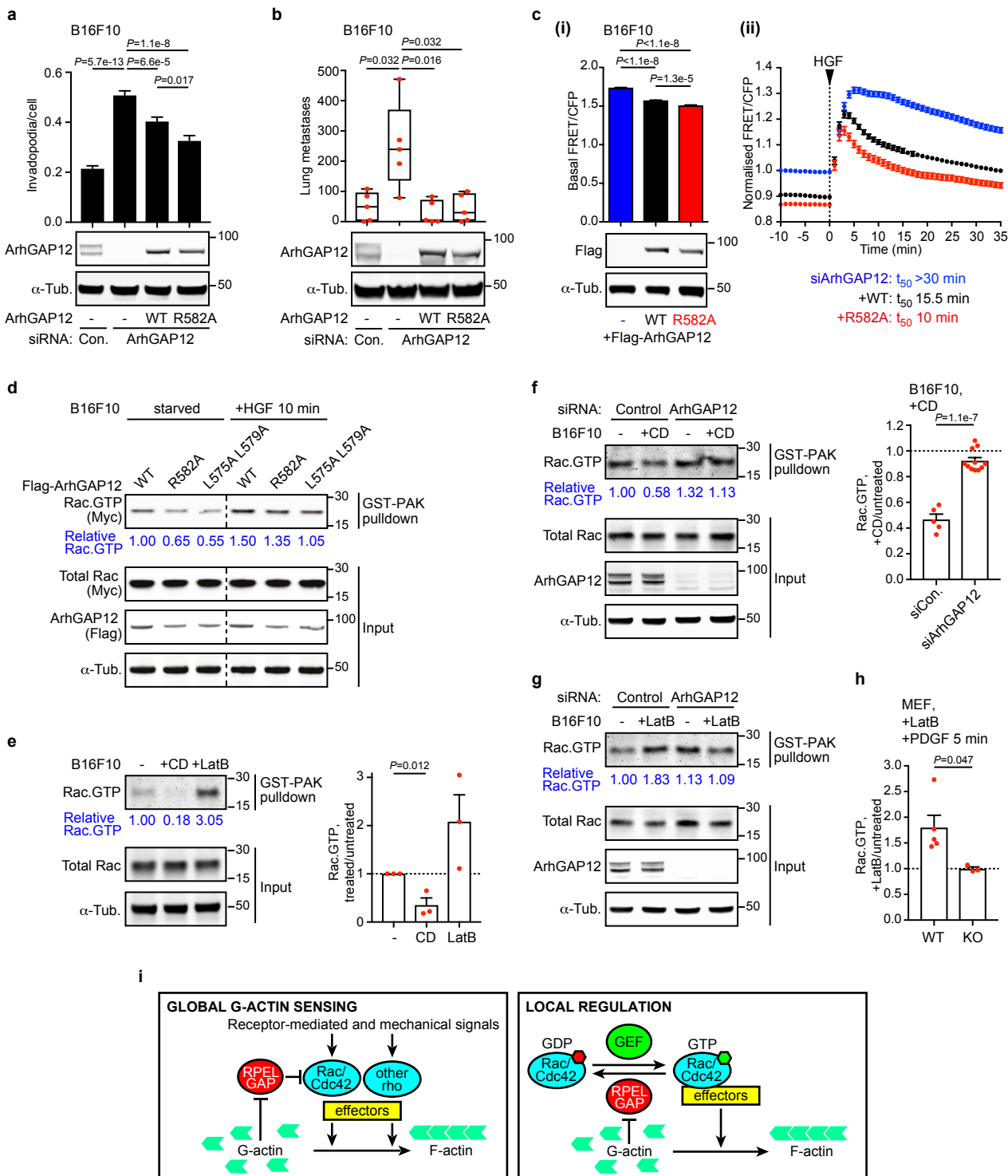
FIGURE 7

Table 1 Crystallographic data collection and structure refinement statistics

ArhGAP12•G-actin (6GVC)	
Data collection	
Space group	P 2 ₁
Cell dimensions	
<i>a</i> , <i>b</i> , <i>c</i> (Å)	101.6, 130.2, 109.3
α , β , γ (°)	90, 111.1, 90
Resolution (Å)	54.13 - 2.6 (2.69 - 2.60) ^a
<i>R</i> _{merge}	0.17 (0.77) ^a
<i>I</i> / σ <i>I</i>	10.82 (1.66) ^a
Completeness (%)	99.43 (95.83) ^a
Redundancy	6.2 (3.4) ^a
Refinement	
Resolution (Å)	54.13 - 2.6 (2.69 - 2.60) ^a
No. reflections	81 098 (7 746)
<i>R</i> _{work}	0.208 (0.317)
<i>R</i> _{free}	0.252 (0.359)
No. atoms	
Protein	17,894
Ligand/ion	268
Water	182
<i>B</i> -factors	
Actin	48.5/47.5/53.0/52.8
ArhGAP12	55.3/54.6/56.0/55.0
Ligand/ion	53.2
Water	42.5
R.m.s. deviations	
Bond lengths (Å)	0.002
Bond angles (°)	0.52
Ramachandran	
Favored (%)	97.45
Allowed (%)	2.51
Outliers (%)	0.04

One crystal was used for the structure

^a Values in parentheses are for highest-resolution shell